

# Image reconstruction method for electrical capacitance tomography using adaptive simulated annealing algorithm

Cite as: Rev. Sci. Instrum. 92, 105009 (2021); doi: 10.1063/5.0059296

Submitted: 8 June 2021 • Accepted: 1 October 2021 •

Published Online: 18 October 2021



View Online



Export Citation



CrossMark

Lifeng Zhang and Menghan Zhang<sup>a)</sup>

## AFFILIATIONS

Department of Automation, North China Electric Power University, Baoding 071003, China

<sup>a)</sup>Author to whom correspondence should be addressed: 2192216112@ncepu.edu.cn

## ABSTRACT

Image reconstruction of electrical capacitance tomography (ECT) is an ill-posed inverse problem. The simulated annealing (SA) algorithm is suitable for the solution of the ECT inverse problem. However, selection of related parameters of the SA algorithm will influence the reconstruction performance of ECT. We present an ECT image reconstruction method based on the adaptive simulated annealing (ASA) algorithm. We adopt the bat algorithm in the new solution generation strategy of the ASA algorithm. Moreover, the definition of the energy function introduces the sparsity of the reconstructed image. As a result, an adaptive annealing strategy is proposed to select the appropriate annealing rate. We made reconstructed image comparisons among linear back-projection, Landweber iteration, SA, and ASA algorithms via simulation and static experiment. Results show that improved reconstructed images can be obtained using the ASA algorithm.

Published under an exclusive license by AIP Publishing. <https://doi.org/10.1063/5.0059296>

## I. INTRODUCTION

Electrical capacitance tomography (ECT) is used for two-phase flow measurement, which can provide the cross-sectional permittivity image for the dielectric media in the pipe.<sup>1–3</sup> However, ECT image reconstruction is nonlinear and ill-posed.<sup>4–6</sup> The precision of the reconstructed image does not meet many application requirements.

At present, many scholars have carried out detailed analysis on the application of electrical capacitance tomography technology. In 1988, Professor Beck from the University of Manchester Science Laboratory successfully developed the first electrical capacitance tomography system composed of eight detection electrodes for the detection of two-phase flow process imaging.<sup>7,8</sup> In the following two years, it was upgraded to an imaging system with 12 array electrodes. The upgraded system used a computer integrated array processor, and the new system was verified by an oil–gas two-phase flow experiment.<sup>9</sup> Huang *et al.* have implanted a multi-processor in the ECT system to measure the oil–water two-phase flow in the transportation pipeline, and the image reconstruction results are good.<sup>10</sup> Mosorov also used the ECT system to detect the burning status of combustible materials, obtaining the combustion parameters through the reconstructed image, and successfully

detected the height and position of the flame in the combustion chamber.<sup>11</sup>

Reconstruction algorithms have been the most studied problem to prompt the industrial applications of ECT.<sup>12–17</sup> In general, they can be classified into non-iterative algorithms such as linear back-projection (LBP) and iterative algorithms such as Landweber iterative algorithm.<sup>18,19</sup> The LBP algorithm is fast but can only provide a qualitative indication for its poor image quality. Iterative algorithms generally have better reconstructed performance, but they are more time-consuming. The least-squares linear inversion and methods based on the gradient of the objective function are most used, which are both local optimization algorithms, and they can only perform local search near the solution domain; thus, there is a lack of more extensive search in the whole solution domain. Consequently, the image reconstruction algorithm of ECT has always been a research hotspot.<sup>20–22</sup>

Different from local optimization reconstruction methods, image reconstruction methods based on global optimization algorithms will search the optimal solution in the complete solution space during the process of ECT image reconstruction. The simulated annealing (SA) algorithm is an effective global optimization method, which is conceived as an analogy of the optimization system in thermodynamics and has been widely used. Meanwhile, SA

is inherently nonlinear and is suitable for the solution of ECT image reconstruction.

SA was introduced in the ECT image, and the improved image reconstruction results were obtained.<sup>23,24</sup> However, due to the intensive calculation of the SA algorithm, the reconstruction process is relatively slow, which cannot meet real-time requirements. Furthermore, the selected values of the related parameter of SA have an influence on the performance of ECT image reconstruction, which is worthy of in-depth study. With regard to this problem, the adaptive simulated annealing (ASA) algorithm is presented in this paper. Compared with the SA algorithm, three improvements have been made. First, the bat algorithm (BA) is introduced in the process of new solution generation.<sup>25–27</sup> Second, the sparsity of the reconstructed image is taken into account in the definition of the energy function. Finally, the adaptive simulated annealing strategy is proposed to select the annealing rate. To verify the performance of the proposed ASA algorithm, image reconstruction by simulation and static experiment has been done with the 12-electrode ECT system and compared with LBP, Landweber iteration, and SA algorithms. Experimental results show that reconstructed images by ASA have improved obviously.

The rest of this paper is organized in the following way: In Secs. II and III, the basis of ECT and the principle of the ASA-based ECT image reconstruction algorithm are introduced, respectively. In Sec. IV, image reconstruction results of the ASA algorithm are shown via simulation and experiment. Conclusions are presented in Sec. V.

## II. BASIS OF ECT

The typical ECT system with 12 electrodes can be shown in Fig. 1, which consists of three parts: electrode array, data acquisition system, and image reconstruction software.

The dielectric constant of the mixed fluid in the tested pipeline will change with the change in fluid distribution. The capacitance value is measured by the array electrode installed on the pipe wall, which will be sent to the computer through the data acquisition system, and the image reconstruction algorithm is used to establish the distribution of fluid in the cross section of the pipeline.

The number of independent measured capacitance data for the sensor with N electrodes can be obtained as

$$M = N(N - 1)/2. \quad (1)$$

Thus, if the ECT system has 12 electrodes, only 66 independent capacitance measurements can be acquired for a whole scanning.

In the ECT system, the electric field distribution equation inside the tested circular pipe is

$$\nabla \cdot [\varepsilon(x, y) \nabla \varphi(x, y)] = 0, \quad (2)$$

where  $\varepsilon(x, y)$  denotes the relative permittivity and  $\varphi(x, y)$  is the electric potential at  $(x, y)$ .

Because the distribution of permittivity is discontinuous, there is no analytic solution for Eq. (2), which can only be solved numerically. When we apply linearization and discretization to Eq. (2), we can get the linearized model as follows:

$$\lambda = SG + e, \quad (3)$$

where  $\lambda$  is the  $m \times 1$ -dimensional normalized capacitance measurement vector,  $S$  is the  $m \times n$  normalized sensitivity coefficient matrix,  $G$  is the  $n \times 1$  normalized image gray value vector,  $e$  is the measurement noise and error vector, and the imaging area is divided into  $n$  pixels. Here,  $m < n$ , and thus, Eq. (3) is underdetermined.

## III. ASA-BASED IMAGE RECONSTRUCTION OF ECT

### A. ECT image reconstruction using SA algorithm

In 1953, the idea of simulated annealing was first proposed; then, the annealing idea was successfully introduced into the field of combinatorial optimization. SA is a kind of random optimization algorithm according to the Monte Carlo iterative solution pattern. The starting point of the SA algorithm comes from thermodynamics, which is based on the analogy between the solid matter annealing process in physics and the solutions of general combinatorial optimization problems.

The SA algorithm is derived from the procedure of solid annealing in thermodynamics. Heat the object to a sufficient temperature, and then cool down the temperature of the object slowly. When heated, the energy of molecules in the object gradually goes up, and the molecules appear disorderly with the temperature ascent. When cooling by inches, the particles are gradually progressively ordered, and then, the particles reach a relatively balanced state of internal energy at every temperature. Finally, when the temperature drops to the room temperature, the internal molecular energy

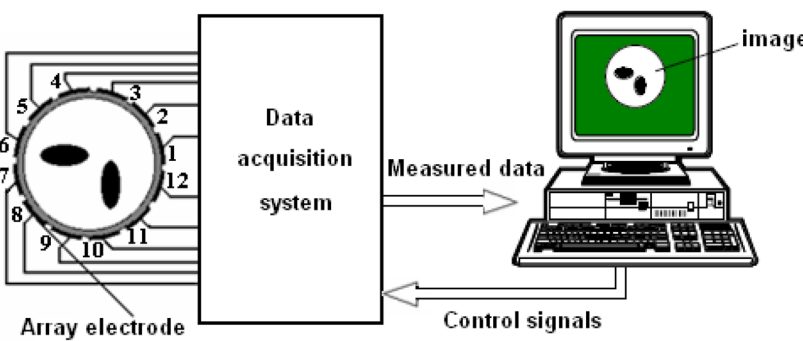


FIG. 1. Structure of the ECT system.

reaches the ground state, and hence, the internal energy is reduced to a minimum.

Thermodynamics theory can be applied to statistical problems and solve the inverse problem of ECT by combining the solid annealing procedure and the global optimization problem. In the SA-based ECT image algorithm, the particle energy is equivalent to the value of some objective function, and the temperature evolves into the adjusted parameters. Setting initial solution and initial value of adjusted parameters, with the continuous decrease of the temperature parameter, it randomly searched the optimal solution of the objective function in the whole solution domain, combining with the characteristics of the parameter that jumps suddenly, that is, the local optimal solution can jump out probabilistically and then eventually tend to the global optimal solution. The current solution at the end of the algorithm is the approximate optimal solution.

The SA algorithm consists of three parts, that is, initial solution, objective function, and solution space. The detailed steps of the image reconstruction method of ECT based on the SA algorithm are described as follows, the flowchart of which is illustrated in Fig. 2:

Step 1: Setting the initial value of the image. The initial value of the image will affect the iteration number of the algorithm. Generally, it can be randomly generated. In order to improve efficiency and reduce time consumption, the solution of the algebra reconstruction technique is selected as the initial value.

Step 2: Initializing algorithm parameters and defining the energy function of the SA algorithm as follows:

$$E = \frac{\sum_{i=1}^n (x_i - x'_i)^2}{n}, \quad (4)$$

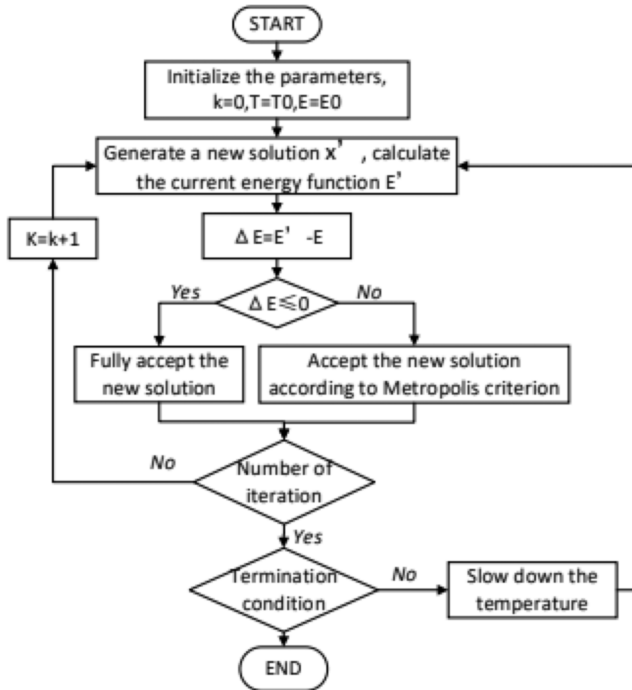


FIG. 2. Flowchart of the SA-based ECT image reconstruction algorithm.

where  $x_i$  and  $x'_i$  are the pixel gray of the original image and the predicted one, respectively.

Step 3: Generating a new solution randomly and calculating the energy difference according to Eq. (5),

$$\Delta E = E' - E, \quad (5)$$

where  $E'$  and  $E$  represent the energy function value corresponding to the solution of the previous iteration and current solution, respectively.

Step 4: Deciding whether or not to accept the new solution by Metropolis criteria, which is shown in Eq. (6),

$$P(\Delta E) = \begin{cases} 1, & \Delta E \leq 0, \\ \exp\left(-\frac{\Delta E}{T}\right), & \Delta E > 0, \end{cases} \quad (6)$$

where  $T$  is the current temperature.

Step 5: Decreasing the temperature according to the temperature decay function and judging whether termination temperature is reached. The temperature decay function is given in the following equation:

$$T_{k+1} = \alpha T_k, \quad (7)$$

where  $T_k$  is the temperature before cooling,  $T_{k+1}$  is the temperature after cooling, and  $\alpha$  is the cooling coefficient, which is a positive number less than 1.

## B. ASA-based image reconstruction algorithm

To accelerate the convergence speed of the SA algorithm and find the optimal solution of ECT image reconstruction, the ASA algorithm for image reconstruction of ECT is presented. Compared with the SA algorithm, three improvements of the ASA algorithm for ECT image reconstruction have been made, which are listed as follows.

### 1. New solution generation strategy

The new solution generation strategy of the SA algorithm can affect the accuracy and speed of image reconstruction for ECT. Generally, the new solution is generated randomly, which is not conducive to improving the search efficiency. In the ASA algorithm, the bat algorithm (BA) is adopted in search of the optimal solution through random flight iteration. The BA algorithm is the population-based stochastic global optimization technology and one kind of new swarm intelligence bionic algorithm to simulate the natural process of bat population hunting.

The principle of BA is described as follows: there are random flight speed and position, which is also the solution to the problem for each bat. Different bats have their own wavelengths, frequencies, loudness, and pulse emission rates. The swarm of bats sends out sound pulses of a certain frequency, then determines the position of prey or obstacles based on echolocation, and successfully forages in the dark. The dynamic flight behavior of the swarm of bats is controlled by the coordination-based technology, which can balance and adjust the relevant parameters of the algorithm in order to obtain the optimal solution of the BA.

Let the position of the  $i$ th bat at time  $t$  be  $x_i^t$  and the velocity be  $v_i^t$ . The update formulas are shown in Eqs. (8)–(10),

$$f_i = f_{\min} + (f_{\max} - f_{\min})\beta, \quad (8)$$

$$v_i^t = v_i^{t-1} + (x_i^t - x_*) f_i, \quad (9)$$

$$x_i^t = x_i^{t-1} + v_i^t, \quad (10)$$

where  $f_i$  represents the sound wave frequency emitted by the  $i$ th bat at the current moment and  $f_{\min}$  and  $f_{\max}$  are the minimum and maximum value of  $f_i$ , respectively.  $\beta$  is a randomly distributed number between 0 and 1, and  $x_*$  is the best solution currently found. At the beginning, the frequency of each bat is randomly assigned.

The new solution generation strategy in the ASA algorithm relies on the idea of the bat algorithm to iteratively search for the optimal solution. Local new solutions are generated by randomly flying around the current optimal solution, and the search process is simulated as a process of individual movement of bats. This new solution generation method considers the current optimal solution and hence strengthens the local search capability, and the accuracy and effectiveness have been greatly improved.

## 2. Energy function

In thermodynamics, if the object keeps lower temperature, the energy is also lower. When the temperature reaches low enough, the object will begin to condense and crystallize, and the system has the lowest energy in the crystalline state. With the decrease of control parameters, the cooling process continues. Meanwhile, the change in energy corresponds to the change in the objective function value, and the lowest energy state means optimal solution. The energy function of the ASA algorithm is defined as

$$E = \min(\|C - SG\|_2 + \mu \cdot D(G)), \quad (11)$$

where  $\mu$  is the weight coefficient and  $D(G)$  is the weighted total difference of the ECT reconstructed image, which is used to describe the sparsity of the image both in horizontal and vertical directions, as is shown in Fig. 3.  $D(G)$  is defined as

$$D(G) = \sum_i \sum_j (|G_{i+1,j} - G_{i,j}| + |G_{i,j+1} - G_{i,j}|). \quad (12)$$

The digital image storage is in the form of a two-dimensional matrix (a grayscale image is a two-dimensional matrix, and a color image is a multiple 2D matrix). The sparsity of the image can be

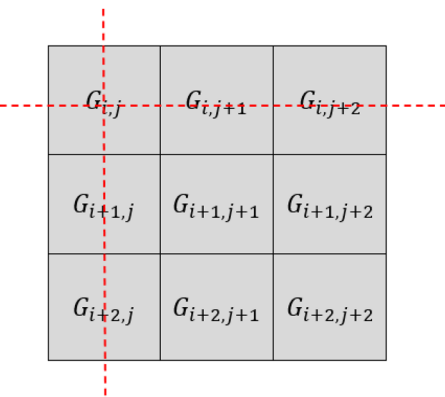


FIG. 3. The weighted total difference of the image gray.

simply understood as some coefficients with large values that concentrate most of the energy and information of the image, which means that a small number of bits can be used to represent the image. As shown in Eq. (11), the definition of the energy function considers the sparse characteristics of the ECT reconstructed images, which is beneficial to improve the reconstructed images of ECT under the same projection data.

## 3. Simulated annealing speed

Aiming at the problem that the optimization accuracy and the convergence speed cannot be balanced, the strategy of selection of simulated annealing speed is improved in the ASA algorithm, which makes it more effective to utilize the SA algorithm's global search capability and accelerate the evolution time.

The improved annealing strategy presents an exponential decay of the weight, being characterized by a rapid decay in the initial stage and a gradual decay in the later stage, which is a development process that conforms to the laws of biological cognition. The exponential decay weight mechanism has a larger weight decay step in the initial stage, which can increase the search area and improve the strong global search ability. The option value decay step is reduced later, causing the update speed of new solutions to slow down, which can ensure better local search, avoid the algorithm oscillation near the local optimal solution caused by the linear attenuation of the weight, and improve the stability of the algorithm convergence.

The temperature attenuation function of the SA algorithm is defined as Eq. (7), and the corresponding temperature attenuation function of ASA is as follows:

$$T_{k+1} = w \cdot \alpha T_k = w \cdot \alpha^k \cdot T_0, \quad (13)$$

where  $w$  is the weight coefficient;  $\alpha$  is the cooling coefficient, which is a positive number less than 1; and  $k$  is the number of cooling times.

The weight factor  $w$  in the temperature attenuation function is a key factor to combine the global exploration capability and local optimization capability of the ASA algorithm. During the iteration process, the difference between  $E_i$  and  $E_{i-1}$  is calculated, and the weight is classified according to the energy difference as follows:

- (a)  $\Delta E = E' - E < 0$  The corresponding energy under the new solution is smaller than the energy corresponding to the previous solution. According to the definition of the energy function, the current solution is closer to the optimal value. At this time, the individual value should be changed in a smaller temperature range to explore the local optimal value. The weight coefficient  $w$  is randomly selected from the range between 0.8 and 1.2.
- (b)  $\Delta E = E' - E = 0$  The current solution is in the general position, just let it approach the optimal position according to the original algorithm, and the inertia weight coefficient  $w$  is set to 1.
- (c)  $\Delta E = E' - E > 0$  The energy under the new solution is greater than that of the previous solution, which means the current solution position is not ideal. As a result, the inertia weight coefficient  $w$  is randomly selected from the range of 0.3–0.6 or 1.3–1.6 with a probability of 0.5, through which other optimal locations can be searched fast and enhance the global optimization capability.

Using this random weight selection strategy, the weight is adjusted randomly according to the magnitude of the energy difference, which not only ensures the algorithm has higher solution accuracy but also ensures that the algorithm has a faster convergence rate.

#### IV. RESULTS AND ANALYSIS

##### A. Simulation results

A simulation experiment was carried out for the ASA-based algorithm for ECT image reconstruction. Oil-gas two-phase simulation flow patterns were set, and the relative permittivity of gas and oil are 1 and 3, respectively. A 12-electrode ECT sensor is used in the simulation experiment, which is shown in Fig. 4.

The simulation software used is Matlab finite element simulation software developed by the research group. The imaging area is divided into 12 layers by triangular meshing, a total of 1728 units. The pipe wall is divided into three layers, and the shielding layer and the pipeline are divided into two layers. The inner diameter of the pipe is set to 62.5 mm, the outer radius of the pipe is 75 mm, and the radius of the shielding layer is 85 mm. The pipe segmentation diagram is shown in Fig. 5. Bubbly flow, cross flow, laminar flow, and annular flow were used for simulation reconstruction.

Reconstructed images using the ASA algorithm were compared with LBP, Landweber iteration, and SA algorithms, which can be seen in Fig. 6. The iteration number of the Landweber algorithm is taken as 150 in this paper. The parameters of the SA algorithm and the ASA algorithm are initial temperature  $T_0 = 1000$ , termination temperature  $T_f = 0.001$ , cooling rate  $\alpha = 0.85$ , and the number of iterations at the current temperature  $L = 25$ .

From the reconstructed images shown in Fig. 6, it can be seen that for the studied six flow patterns, all the reconstructed images of LBP have artifacts and there are serious distortions in flow patterns *a–d*, which are unacceptable in practical applications. Using the Landweber iterative algorithm, the reconstructed images were obviously improved compared with the LBP algorithm. Reconstructed results of flow patterns *a*, *b*, *e*, and *f* are acceptable, but there still exist artifacts and shape distortion. There are serious distortions in

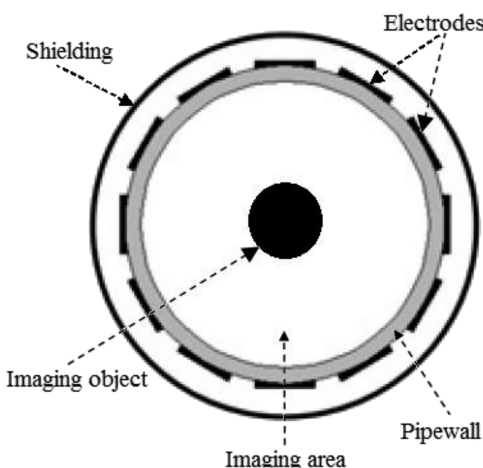


FIG. 4. ECT sensor with 12 electrodes.

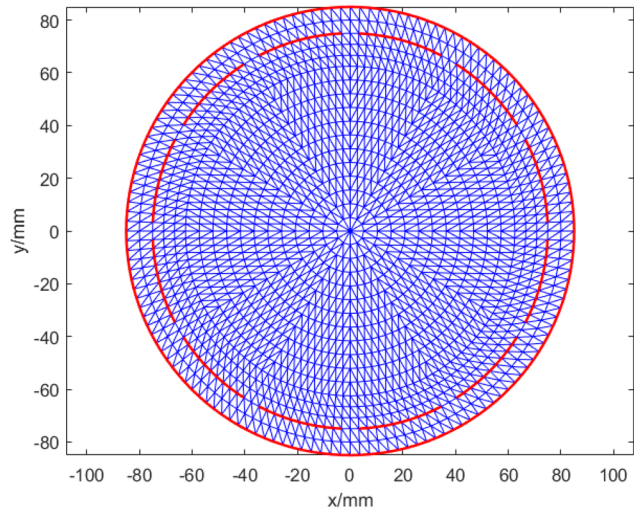


FIG. 5. Pipe segmentation diagram.

the reconstructed images for flow patterns *c* and *d* using the Landweber iterative algorithm, which reflects the poor reconstruction capability for complex flow patterns in which many objects are close to each other or objects with sharp edge.

At the same time, it can be seen that for the reconstructed images of the SA algorithm shown in Fig. 6, the accuracy and shape fidelity of reconstructed images of flow patterns *a*, *b*, and *d* are greatly improved in comparison with those of LBP and Landweber iterative algorithms. The reconstructed objects are very close to the real distributions in the aspects of size, position, and shape. Different objects can be separated distinctively. As for flow patterns *c*, *e* and *f*, there are large distortions in reconstructed images, which are unacceptable. Finally, it can be shown that the reconstructed results of the ASA algorithm have the best quality compared with the other three algorithms for all the flow patterns. The size, shape, and position of the target objects in the reconstructed images tend to the true distribution of the original flow pattern, which proves the effectiveness of the ASA-based ECT image reconstruction algorithm.

At the same time, the quality of the reconstructed images is evaluated quantitatively using the index of relative image error (*RE*) and the correlation coefficient (*CC*). The definitions of *RE* and *CC* are given as follows:

$$RE = \frac{\|\mathbf{G}^* - \mathbf{G}\|_2}{\|\mathbf{G}\|_2}, \quad (14)$$

$$CC = \frac{\sum_{i=1}^n (\mathbf{G}^* - \bar{\mathbf{G}}^*) \cdot (\mathbf{G} - \bar{\mathbf{G}})}{\sqrt{\sum_{i=1}^n (\mathbf{G}^* - \bar{\mathbf{G}}^*)^2 \cdot (\mathbf{G} - \bar{\mathbf{G}})^2}}, \quad (15)$$

where  $\mathbf{G}$  and  $\mathbf{G}^*$  are the gray value of the actual flow pattern and the gray value of the reconstructed image, respectively.  $\bar{\mathbf{G}}$  and  $\bar{\mathbf{G}}^*$  are the mean values of  $\mathbf{G}$  and  $\mathbf{G}^*$ , respectively.

If the reconstructed images have better quality, *RE* will be smaller and *CC* will be larger. The values of *RE* and *CC* for the reconstructed images using four algorithms in Fig. 6 are calculated and listed in Tables I and II, respectively.

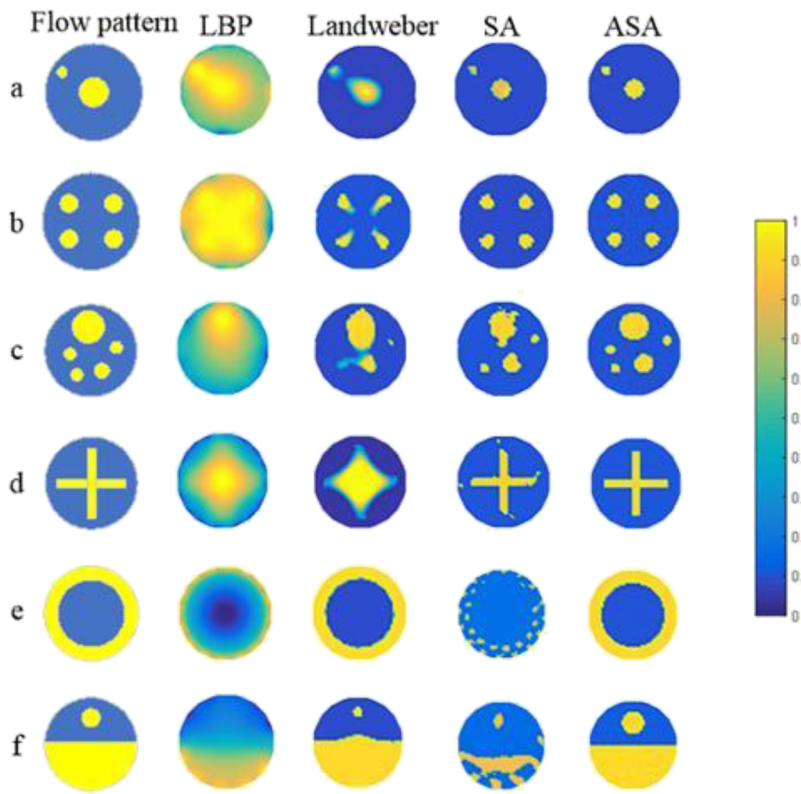


FIG. 6. Reconstructed images of six flow patterns.

It can be shown from Tables I and II that the quality index of reconstructed images using the ASA algorithm reaches the best. For the six flow patterns in Fig. 6, the RE of each reconstructed image is the lowest, while the CC is the largest compared with the other three algorithms.

TABLE I. RE of reconstructed images in Fig. 6.

Flow pattern	LBP	Landweber	SA	ASA
a	0.9536	0.6442	0.4547	0.004801
b	0.9493	0.6121	0.3045	0.037717
c	0.8813	0.6872	0.5771	0.030572
d	0.8703	0.8910	0.11164	0.003152
e	0.4685	0.1950	0.97522	0.002259
f	0.4269	0.4112	2.3174	0.021848

TABLE II. CC of reconstructed images in Fig. 6.

Flow pattern	LBP	Landweber	SA	ASA
a	0.3891	0.7673	0.9752	0.9998
b	0.2784	0.7818	0.9522	0.9790
c	0.5018	0.7147	0.8439	0.9498
d	0.5035	0.6235	0.9242	0.9989
e	0.8276	0.9619	0.3250	0.9989
f	0.7990	0.8056	0.3653	0.9398

TABLE III. The computation time of each algorithm used in Fig. 6 (unit: s).

Flow pattern	LBP	Landweber	SA	ASA
a	0.005237	0.629245	2.765400	1.207600
b	0.004429	0.330078	1.851661	0.899235
c	0.005534	0.408902	1.922872	1.283757
d	0.007728	0.375576	3.090900	1.24686
e	0.007956	0.455244	0.997783	1.593715
f	0.004414	0.335146	1.725682	1.561260

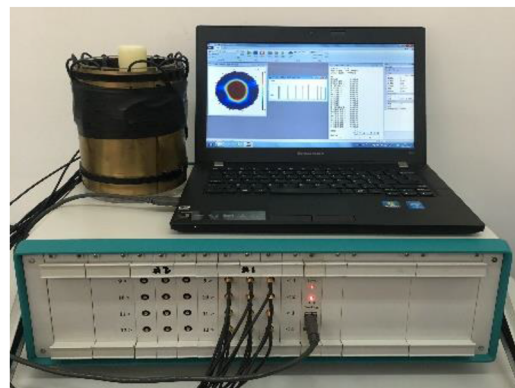


FIG. 7. Digital ECT system.

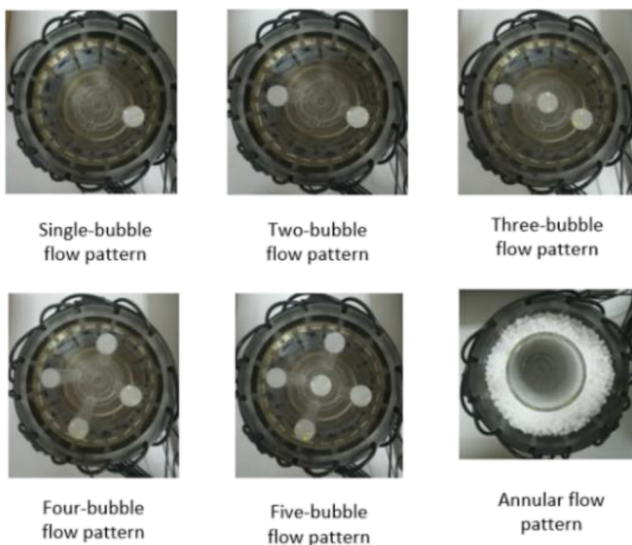


FIG. 8. Static experiments.

In addition, the consuming time of each algorithm in Fig. 6 was computed and is listed in Table III.

LBP and SA algorithms have the shortest and longest computation time, respectively. SA and ASA algorithms both have longer computing time than the Landweber iterative algorithm, and the ASA algorithm consumes less time than the SA algorithm, which proves its effectiveness in accelerating the convergence of the SA algorithm.

### B. Static experiment and results

A static experiment was also carried out and the digital ECT system is used, which is shown in Fig. 7. There are 24 channels in the ECT system, which are designed for the use up to two layers of the ECT sensor with 12 electrodes. The online image reconstruction speed can reach 120 fps. The sensor used in the static experiment is a circular Perspex glass pipe with an inner diameter of 60 mm, and the copper shield is used.

Air and plastic particles are used for the empty field and full field calibration, respectively.

Six distributions used for performance evaluation were set up, which are shown in Fig. 8. Plastic rods with a diameter of 10 mm

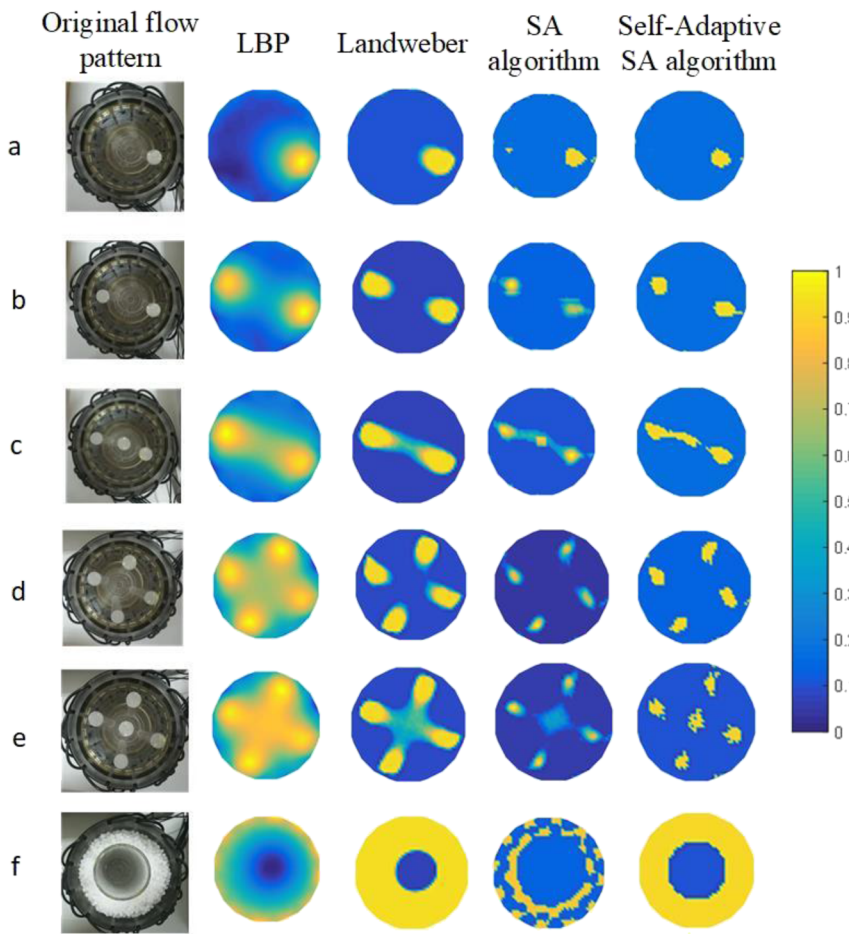


FIG. 9. Static experimental results.

**TABLE IV.** The computation time of each algorithm used in Fig. 9 (unit: s).

Flow pattern	LBP	Landweber	SA	ASA
a	0.004 294	0.363 288	1.320 927	0.646 437
b	0.004 340	0.381 839	1.489 503	0.685 048
c	0.004 152	0.393 844	1.913 469	0.847 070
d	0.004 821	0.360 816	1.932 681	0.843 092
e	0.004 204	0.406 867	1.646 647	0.733 280
f	0.004 300	0.362 262	1.242 712	0.642 144

are used to simulate bubbly flow, and a hollow plastic pipe with an inner diameter of 30 mm and a thickness of 2 mm is used to simulate the annular flow. The various flow patterns shown in Fig. 8 are used to test the reconstruction effect of the ASA algorithm on simple flow patterns, complex flow patterns, laminar flow, and annular flow. The reconstructed images of the static experiment can be seen in Fig. 9, which were compared with LBP, Landweber iteration, and SA algorithms. The parameters employed in different algorithms were consistent with those in the simulation experiment. In addition, the time consumption of image reconstruction under different algorithms in the static experiment is also compared, and the comparison results are shown in Table IV.

For the simple distributions *a*, *b*, *d*, and *f*, the LBP algorithm can only provide qualitative results with noticeable artifacts in Fig. 9. However, for the complex distributions *c* and *e*, there are serious distortions in the reconstructed images of the LBP algorithm in which the object in the center cannot be detected. The quality of reconstructed images has an obvious improvement compared with the LBP algorithm. The artifacts were significantly reduced, and objects can be clearly separated. While for the complex distributions *c* and *e*, the object in the center area still cannot be detected, causing image distortion. While taking a look at the reconstructed images of SA and ASA algorithms, the reconstructed images were improved greatly and the artifacts are further decreased in comparison with LBP and Landweber iterative algorithms. At the same time, the reconstructed image distortions can be found for distributions *e* and *f*. When it comes to the ASA algorithm, it can be seen from Fig. 9 that the size, position, and shape of objects in the reconstructed images tend to the true distributions. The artifacts were mostly eliminated, and central objects can be detected in distribution *e* under the ASA algorithm. It can be seen from Table IV that the LBP algorithm takes a shorter time for image reconstruction, followed by the Landweber algorithm and the ASA algorithm, and the SA algorithm takes the longest time. The time-consumption of the ASA algorithm is higher than that of the SA algorithm, which improves the timeliness of image reconstruction. However, there is still a large space for improvement when compared with the other two algorithms.

## V. CONCLUSION

The ASA-based ECT image reconstruction algorithm was presented for improving the performance of the SA algorithm for ECT image reconstruction in this paper. Compared with the SA algorithm, the ASA algorithm has better optimal performance and less consuming time. Both the simulation and experimental results show that the reconstructed images are improved obviously for simple and complex flow patterns in the aspects of size, position, and shape

of objects. In addition, the disadvantage of the ASA algorithm is that it takes longer time than traditional algorithms, and there is still space for improvement in meeting the real-time requirements of image reconstruction. We can note that this method can also be used in other tomography techniques such as electrical resistance tomography.

## ACKNOWLEDGMENTS

The authors acknowledge the National Natural Science Foundation of China (Grant No. 61973115).

## AUTHOR DECLARATIONS

### Conflict of Interest

The authors have no conflicts to disclose.

## DATA AVAILABILITY

The data that support the findings of this study are available within the article.

## REFERENCES

- X. Deng, D. Chen, and W. Yang, "Study on electrodynamic sensor of multimodality system for multiphase flow measurement," *Rev. Sci. Instrum.* **82**, 124701 (2011).
- W. Zhang, C. Wang, W. Yang, and C.-H. Wang, "Application of electrical capacitance tomography in particulate process measurement a review," *Adv. Powder Technol.* **25**, 174–188 (2014).
- F. R. Moreira da Mota, D. J. Pagano, and M. Enricone Stasiak, "Water volume fraction estimation in two-phase flow based on electrical capacitance tomometry," *IEEE Sens. J.* **18**, 6822–6835 (2018).
- Z. Hao, Z. Cui, S. Yue, and H. Wang, "Amplitude demodulation for electrical capacitance tomography based on singular value decomposition," *Rev. Sci. Instrum.* **89**, 074705 (2018).
- J. Lei, H. Mu, Q. Liu, Z. Li, S. Liu, and X. Wang, "Tensor-based dynamic reconstruction method for electrical capacitance tomography," *Meas. Sci. Technol.* **28**, 035403 (2017).
- E. Al Hosani, M. Zhang, and M. Soleimani, "A limited region electrical capacitance tomography for detection of deposits in pipelines," *IEEE Sens. J.* **15**, 6089–6099 (2015).
- W. Q. Yang and T. York, "New AC-based capacitance tomography system," *Meas. Sci. Technol.* **19**, 47–53 (2008).
- A. Gonzalez-Nakazawa, J. C. Gamio, and W. Q. Yang, "Transient processes and noise in a tomography system: An analytical case study," *IEEE Sens. J.* **5**, 321–329 (2005).
- C. G. Xie, S. M. Huang *et al.*, "Experimental evaluation of capacitance tomographic flow imaging systems using physical models," *IEE Proc. - Circuits, Devices Syst.* **141**, 357–368 (2009).
- S. M. Huang, R. G. Green *et al.*, "A high frequency stray-immune capacitance transducer based on the charge transfer principle," *IEEE Trans. Instrum. Meas.* **37**, 368–373 (1992).
- V. Mosorov, D. Sankowski, L. Mazurkiewicz, and T. Dyakowski, "The best-correlated pixels method for solid mass flow measurements using electrical capacitance tomography," *Meas. Sci. Technol.* **13**, 1810–1814 (2002).
- Z. H. Guo, Z. Kan, D. C. Lv, and F. Q. Shao, "Regional regularization method for ECT based on spectral transformation of Laplacian," *Rev. Sci. Instrum.* **87**, 104709 (2016).
- M. Soleimani and W. R. B. Lionheart, "Nonlinear image reconstruction for electrical capacitance tomography using experimental data," *Meas. Sci. Technol.* **16**, 1987–1996 (2005).

- <sup>14</sup>Z. Cui, Q. Wang, Q. Xue, W. Fan, L. Zhang, Z. Cao, B. Sun, H. Wang, and W. Yang, "A review on image reconstruction algorithms for electrical capacitance/resistance tomography," *Sens. Rev.* **36**, 429–445 (2016).
- <sup>15</sup>Q. Guo, M. Ye, W. Yang, and Z. Liu, "A machine learning approach for electrical capacitance tomography measurement of gas-solid fluidized beds," *AIChE J.* **65**, e16583 (2019).
- <sup>16</sup>J. Lei, Q. Liu, and X. Wang, "Deep learning-based inversion method for imaging problems in electrical capacitance tomography," *IEEE Trans. Instrum. Meas.* **67**, 2107–2118 (2018).
- <sup>17</sup>J. Ye, H. Wang, and W. Yang, "Image recovery for electrical capacitance tomography based on low-rank decomposition," *IEEE Trans. Instrum. Meas.* **66**, 1751–1759 (2017).
- <sup>18</sup>W. Q. Yang, D. M. Spink, T. A. York, and H. McCann, "An image-reconstruction iteration method for electrical-capacitance tomography," *Meas. Sci. Technol.* **10**, 1065–1069 (1999).
- <sup>19</sup>J. Sun, W. Tian, H. Che, S. Sun, S. Gao, L. Xu, and W. Yang, "Proportional-integral controller modified Landweber iterative method for image reconstruction in electrical capacitance tomography," *IEEE Sens. J.* **19**, 8790–8802 (2019).
- <sup>20</sup>S. X. Sun, Q. Zhao, S. Liu, H. X. Zhu, Y. Ju, M. Zhang, and J. Liu, "Sensitivity guided image fusion for electrical capacitance tomography," *IEEE Trans. Instrum. Meas.* **70**, 4502312 (2021).
- <sup>21</sup>Q. Guo, X. Li, B. Hou, G. Mariethoz, M. Ye, W. Yang, and Z. Liu, "A novel image reconstruction strategy for ECT: Combining two algorithms with a graph cut method," *IEEE Trans. Instrum. Meas.* **69**, 804–814 (2020).
- <sup>22</sup>Z. H. Xia, Z. Q. Cui, Y. X. Chen, Y. F. Hu, and H. X. Wang, "Generative adversarial networks for dual-modality electrical tomography in multi-phase flow measurement," *Measurement* **173**, 108608 (2020).
- <sup>23</sup>C. Ortiz-Alemán and R. Martin, "Inversion of electrical capacitance tomography data by simulated annealing: Application to real two-phase gas-oil flow imaging," *Flow Meas. Instrum.* **16**, 157–162 (2005).
- <sup>24</sup>C. Ortiz-Aleman, R. Martin, and J. C. Gamio, "Reconstruction of permittivity images from capacitance tomography data by using very fast simulated annealing," *Meas. Sci. Technol.* **15**, 1382–1390 (2004).
- <sup>25</sup>B. Vedik and A. K. Chandel, "Optimal PMU placement for power system observability using Taguchi binary bat algorithm," *Measurement* **95**, 8–20 (2017).
- <sup>26</sup>L. J. Liu, S. N. Luo, F. Guo, and S. Y. Tan, "Multi-point shortest path planning based on an improved discrete bat algorithm," *Appl. Soft Comput.* **95**, 106498 (2020).
- <sup>27</sup>H. G. Tang, W. Sun, H. S. Yu, A. P. Lin, and M. Xue, "A multirobot target searching method based on bat algorithm in unknown environments," *Expert Syst. Appl.* **141**, 112945 (2020).